

# Nonreciprocal wave-mediated interactions power a classical time crystal

Mia C. Morrell\*, Leela Elliott\*, and David G. Grier  
*Department of Physics and Center for Soft Matter Research,  
 New York University, New York, New York 10003, USA*  
 (Dated: December 24, 2025)

An acoustic standing wave acts as a lattice of evenly spaced potential energy wells for sub-wavelength-scale objects. Trapped particles interact with each other by exchanging waves that they scatter from the standing wave. Unless the particles have identical scattering properties, their wave-mediated interactions are nonreciprocal. Pairs of particles can use this nonreciprocity to harvest energy from the wave to sustain steady-state oscillations despite viscous drag and the absence of periodic driving. We show in theory and experiment that a minimal system composed of two acoustically levitated particles can access four distinct dynamical states, two of which are emergently active steady states. Under some circumstances, these emergently active steady states break spatiotemporal symmetry and therefore constitute a classical time crystal.

Waves exert forces on scatterers. Scattered waves coalesce collections of independent scatterers into self-organizing dynamical systems by mediating interparticle interactions [1–7]. Wave-mediated pair interactions are not constrained by Newton’s third law because the scatterers are not a closed system: scattered waves can carry away momentum, causing pairs of interacting particles to recoil [8–11]. The nonreciprocity of wave-mediated interactions allows scatterers to capture energy from the wave and to transduce it into collective motion, thereby endowing an otherwise passive system with the defining characteristics of active matter [12–16]. This form of activity is distinctive because it is not an inherent property of the individual particles, but instead is an emergent property of the particles’ configuration [11].

Here we demonstrate that emergent activity can take the form of sustained oscillations in an acoustically levitated array of particles. Nonreciprocal wave-mediated interactions continuously transfer energy from the levitator’s standing wave into the lattice’s normal modes without requiring periodic driving. We show both in theory and through experiments that a minimal system of two acoustically levitated particles can use this mechanism to access a variety of dynamical states, including actively sustained steady states [17–19], one of which is a continuous classical time crystal [10, 20, 21]. Figure 1(a) shows such a time crystal in action.

A classical time crystal is a dynamical system whose spatiotemporal symmetry is spontaneously broken. The time crystal restores discrete spatiotemporal symmetry through the emergence of a linearly stable limit cycle [10]. Such a time crystal is said to be continuous if the system’s governing equations are invariant under continuous time translation, in which case its oscillation frequency is an emergent property. This contrasts with discrete time crystals that oscillate at harmonics or subharmonics of an imposed driving frequency [22].

The levitator used for this study is based on the popular TinyLev2 design [23], which operates at 40 kHz in air and creates a linear array of pressure nodes with a lattice constant of 4.3 mm. Each node acts as a three-dimensional potential energy well for a millimeter-scale

bead [24, 25] and exerts a nearly Hookean restoring force whose stiffness depends on the bead’s properties. Trapped beads interact by exchanging scattered waves, as depicted schematically in Fig. 1(b). Their resulting motions are recorded with a video camera (Blackfly S, Teledyne Flir) outfitted with a 35 mm  $f/1.4$  lens (Nikon, Nikon) yielding a magnification of  $(139 \pm 1) \mu\text{m}/\text{pixel}$ .

The standing pressure wave along the levitator’s axis,

$$p(z, t) = p_0 \sin(kz) \cos(\omega t), \quad (1)$$

is characterized by its amplitude,  $p_0$ , its frequency,  $\omega$ , and its wave number,  $k = \omega/c_0$ , in a medium of sound speed  $c_0$ . Objects scattering this wave experience time-averaged forces that organize them into a periodic lattice along the wave’s axis,  $\hat{z}$ , even if they have different wave-scattering characteristics. Heterogeneity in the trapped particles’ properties constitutes quenched disorder in the levitated array and creates a context for nonreciprocal dynamics [11] that has not been addressed previously.

A sphere labeled  $j$  and located at  $z_j$  within the standing wave experiences a time-averaged force originally formulated by Gor’kov [26–28],

$$\mathbf{F}_j(kz_j) = -\frac{\pi}{3} F_0 A_j x_j^3 \sin(2kz_j) \hat{z}, \quad (2a)$$

whose scale,

$$F_0 = \frac{p_0^2}{\rho_0 \omega^2}, \quad (2b)$$

is proportional to the acoustic energy density in a medium of mass density  $\rho_0$ . Our levitator’s calibrated [25] force scale is  $F_0 = (25.2 \pm 0.3) \mu\text{N}$ . The Gor’kov force on a sphere also depends on the sphere’s radius,  $a_j$ , relative to the wavelength of sound,

$$x_j = k a_j, \quad (2c)$$

as well as its density,  $\rho_j$ , and the ratio of its isentropic compressibility,  $\kappa_j$ , to that of the medium,  $\kappa_0$ . These material properties contribute to a dimensionless coupling constant [11],

$$A_j = f_{0,j} + f_{1,j}, \quad (2d)$$

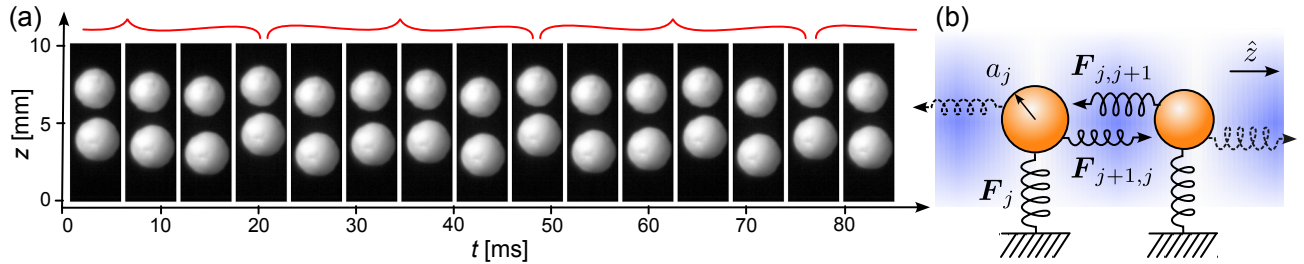


FIG. 1. (a) Experimental realization of a steady-state time crystal composed of two millimeter-scale spheres of expanded polystyrene levitated in air by an acoustic standing wave at 40 kHz. Images captured at 170 frames/s reveal sustained oscillations without periodic driving and despite dissipation due to viscous drag. Curly braces denote twice the 16 ms predicted period of the 61 Hz antisymmetric mode. (b) Model for the forces acting on spheres localized at the nodes of an acoustic standing wave, including restoring forces,  $\mathbf{F}_j$ , and nonreciprocal interparticle forces,  $\mathbf{F}_{ij}$  and  $\mathbf{F}_{ji}$ . Dashed springs represent the possibility of extending the system to more than two particles.

that combines the spheres' monopole (pressure) and dipole (velocity) polarizabilities,

$$f_{0,j} = 1 - \frac{\kappa_j}{\kappa_0} \quad \text{and} \quad (3a)$$

$$f_{1,j} = \frac{\rho_j - \rho_0}{2\rho_j + \rho_0}, \quad (3b)$$

respectively. Rigid spheres ( $\kappa_j \ll \kappa_0$ ) that are denser than the medium ( $\rho_j > \rho_0$ ) tend to be stably trapped at nodes of the pressure field, located at  $kz_j = j\pi$ . This is the case for the expanded polystyrene (EPS) beads depicted in Fig. 1(a) that are sufficiently incompressible relative to air that we set  $f_{0,j} \approx 1$ . The beads' mass density is  $\rho_j = (30.5 \pm 0.2) \text{ kg/m}^3$  [25, 29], relative to  $\rho_0 = (1.204 \pm 0.005) \text{ kg/m}^3$  for air, from which we obtain  $f_{1,j} = 0.471 \pm 0.002$ .

The wave-mediated interaction force was originally formulated by König in 1893 [30] for the special case of identical spheres in a common nodal plane. This result recently has been generalized to accommodate dissimilar spheres at arbitrary positions within the wave [11]. The leading-order generalized König force on sphere  $j$  due to the wave scattered by sphere  $i$ ,

$$\mathbf{F}_{ji}^K(kr_{ji}) = -2\pi F_0 f_{1,i} f_{1,j} x_j^3 x_i^3 \Phi(kr_{ji}) \hat{r}_{ji}, \quad (4a)$$

depends on the spheres' separation,  $\mathbf{r}_{ji} = \mathbf{r}_j - \mathbf{r}_i$ , through the dimensionless geometric factor,  $\Phi(kr)$ . For the special case of spheres trapped in nodes along the axis of a standing wave, the separation dependence reduces to

$$\Phi(kr) = \frac{\cos(kz) + kz \sin(kz)}{(kz)^2}, \quad (4b)$$

which depends only on the trapped spheres' axial separation,  $z$ . The analytic expression in Eq. (4) for the axial König force appears not to have been reported previously and is one of the contributions of this work. Whereas the transverse König interaction falls off as  $r^{-4}$  [11, 24, 30, 31], the axial König force falls off as  $r^{-2}$  and thus is longer-ranged.

Equation (4) is strictly valid only in the Rayleigh regime, which pertains to scatterers that are smaller than the wavelength of sound,  $x_j < 1$ . Comparison with numerical studies [32], however, shows that Eq. (4) captures qualitative features of the inter-particle force for larger spheres in the range  $1 \leq x_j < 3$ .

While Equation (4) is reciprocal under exchange of the indices  $i$  and  $j$  [33, 34], incorporating quadrupolar and octupolar scattering at leading order in  $x_j$  [11] yields corrections,  $\chi_{ji}$ , to the pair interaction,

$$\mathbf{F}_{ji}(kz) = \mathbf{F}_{ji}^K(kz) (1 - \chi_{ji}), \quad (5a)$$

that are nonreciprocal unless spheres  $i$  and  $j$  are identical. For spheres made of the same material, these higher-order corrections reduce to two contributions:

$$\chi_{ji} = \frac{2}{5} \sigma_{ji}(2) + \frac{1}{10} \Delta_{ji}(2), \quad (5b)$$

that depend on the spheres' sizes through

$$\sigma_{ji}(n) = x_j^n + x_i^n \quad \text{and} \quad (5c)$$

$$\Delta_{ji}(n) = x_j^n - x_i^n. \quad (5d)$$

The latter of these factors changes sign under exchange of indices and therefore describes a nonreciprocal contribution to the pair interaction. More generally, Eq. (5d) establishes that spheres of different sizes interact nonreciprocally, as depicted schematically in Fig. 1(b).

Combining the Gor'kov force from Eq. (2) with the generalized axial König interaction from Eq. (5) yields the equations of motion for an array of acoustically levitated spheres trapped at the nodes of a standing wave. The dimensionless displacement of the  $j$ -th sphere from its trap,  $\zeta_j(\tau) = kz_j(t) - j\pi$ , evolves in time according to the system of coupled equations,

$$\nu_j \equiv \dot{\zeta}_j \quad (6a)$$

$$\dot{\nu}_j = -\frac{1}{2} \sin(2\zeta_j) - \Gamma_j \nu_j + \sum_{i \neq j} B_{ji} \Phi(kz_{ji}), \quad (6b)$$

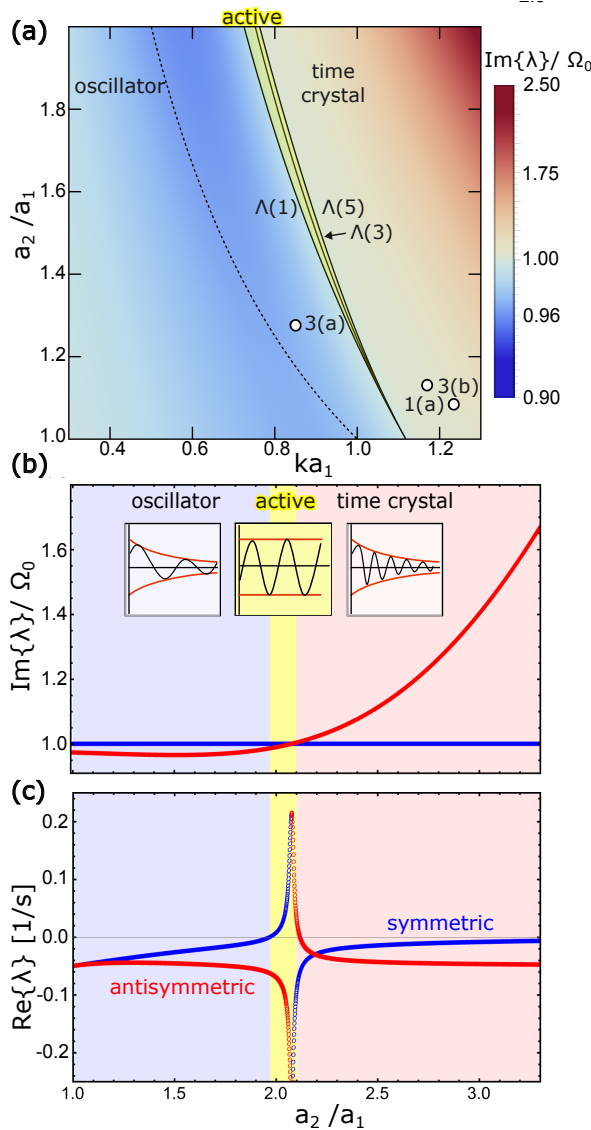


FIG. 2. (a) Dynamical states for a pair of levitated spheres of radii  $a_1$  and  $a_2$ . Dashed curve: Rayleigh limit:  $ka_1, ka_2 \leq 1$ . Solid curves: roots of the stability functions:  $\Lambda(n) = 0$ . Activity surpasses dissipation in the (yellow) region bounded by  $\Lambda(1) = 0$  and  $\Lambda(5) = 0$ . Circles denote experimental conditions from Fig. 1(a) and Fig. 3. Shading represents the frequency of the antisymmetric mode relative to the natural frequency. (b) Frequency and (c) growth rate for the symmetric (blue) and antisymmetric (red) modes for pairs with  $a_1 = 1 \text{ mm}$  ( $ka_1 = 0.732$ ). Activity powers spontaneous emergence of oscillations in the (yellow) region where  $\text{Re}\{\lambda\} \geq 0$ . The steady-state symmetric mode is an active oscillator. The steady-state antisymmetric mode is a time crystal.

where  $kz_{ji} = (j-i)\pi + \zeta_j - \zeta_i$ . Dots in Eq. (6) represent derivatives with respect to the dimensionless time,  $\tau = \Omega_0 t$ , which is scaled by the natural oscillation frequency,

$$\Omega_0 = \sqrt{\frac{F_0 A_j k^4}{2\rho_j}}. \quad (7)$$

For the EPS beads in our system,  $\Omega_0 = (418 \pm 2) \text{ rad/s}$  or  $(66.5 \pm 0.3) \text{ Hz}$ . The interparticle coupling,

$$B_{ji} = -3 \frac{f_{1,j}^2}{A_j} x_i^3 (1 - \chi_{ji}) \hat{r}_{ji} \cdot \hat{z}, \quad (8)$$

is nonreciprocal if the spheres differ in size. Equation (6) is based on the time-averaged Gor'kov and König forces and therefore is time-invariant. For simplicity, we model dissipation by Stokes drag acting on the individual spheres independently in a medium of viscosity  $\eta_0$ . Its influence is characterized by a dimensionless damping rate,  $\Gamma_j = 2\epsilon x_j^{-2}$ , where

$$\epsilon = \frac{9}{4} \frac{k^2 \eta_0}{\rho_j \Omega_0}. \quad (9)$$

The expression for  $\Gamma_j$  can be modified to account for inertial effects in the fluid medium [25, 31, 35, 36] without affecting the functional form of Eq. (6).

The normal modes for a pair of acoustically levitated spheres labeled 1 and 2 are obtained from the Jacobian of the equations of motion,  $\underline{J}(\zeta_1, \zeta_2; \nu_1, \nu_2)$ , by solving the characteristic equation,

$$|\underline{J}(0, 0; \nu_1, \nu_2) - \lambda \underline{I}| = 0, \quad (10)$$

for the eigenvalues,  $\lambda$ , at the fixed point for the Gor'kov force,  $\zeta_1 = \zeta_2 = 0$ .

The full analytic expressions for  $\lambda$  are unwieldy. For clarity, we treat drag as a perturbation [37],  $\epsilon < 1$ , to obtain an approximate expression for the symmetric mode's eigenvalues in units of  $\Omega_0$ :

$$\frac{\lambda_{\pm}^{(s)}}{\Omega_0} = \pm i - \epsilon \frac{\Lambda(1)}{\Lambda(3)} + \mathcal{O}\{\epsilon^2\}. \quad (11a)$$

Similarly, the antisymmetric mode's eigenvalues are

$$\frac{\lambda_{\pm}^{(a)}}{\Omega_0} = \pm i \sqrt{1 - g \Lambda(3)} - \frac{\epsilon}{x_1^2 x_2^2} \frac{\Lambda(5)}{\Lambda(3)} + \mathcal{O}\{\epsilon^2\}. \quad (11b)$$

Equation (11) is suitable for our experimental system because the viscosity of air is  $\eta_0 = 1.825 \times 10^{-5} \text{ Pas}$  [38], so that  $\epsilon = (1.73 \pm 0.01) \times 10^{-3}$ .

The particles' sizes determine the nature of these solutions through stability functions,

$$\Lambda(n) = \left[ 1 - \frac{2}{5} \sigma_{12}(2) \right] \sigma_{12}(n) + \frac{1}{10} \Delta_{12}(2) \Delta_{12}(n), \quad (11c)$$

whose roots establish boundaries between the system's different dynamical states. The frequency of the antisymmetric mode additionally depends on particle size through  $\Lambda(3)$ , and on the particles' composition through

$$g = 3 \frac{\pi^2 - 2}{\pi^3} \frac{f_{1,j}^2}{A_j}, \quad (11d)$$

which has no subscript because the particles in our minimal model are all assumed to be made of the same

material. For the EPS beads used in our experiments,  $g = 0.1148 \pm 0.0001$ .

The normal mode frequencies,  $\Omega_{\pm}^{(s,a)} = \text{Im} \left\{ \lambda_{\pm}^{(s,a)} \right\}$ , are not influenced by drag to leading order in  $\epsilon$ . These modes nevertheless tend to be damped because viscous drag typically removes energy from the system faster than nonreciprocal interactions can replace it. The passive state is a stable fixed point of the dynamics under these conditions. This prediction is consistent with the experimental observation that most randomly selected pairs of spheres remain motionlessly trapped in the acoustic levitator.

Not all systems have overdamped normal modes. For pairs that satisfy  $\Lambda(1)/\Lambda(3) \leq 0$ , for example, the initial growth rate of the symmetric mode is non-negative,  $\text{Re} \left\{ \lambda_{\pm}^{(s)} \right\} \geq 0$ , which means that the system spontaneously breaks into common-mode oscillation. Similarly, the antisymmetric mode grows when  $\Lambda(5)/\Lambda(3) \leq 0$ , leading to spontaneous breathing-mode oscillations. Roots of the stability functions,  $\Lambda(1) = 0$  and  $\Lambda(5) = 0$ , therefore bound the conditions where the system is emergently active. These boundaries are plotted as solid curves in Fig. 2(a). Higher-order contributions to the damping [25] that are not included in Eq. (6) can stabilize the growing modes, which then settle into steady-state oscillation. The active region vanishes for particles of the same size ( $a_1 = a_2$ ), whose interactions are reciprocal.

Regions in Fig. 2(a) are colored by the frequency of the lower-frequency normal mode obtained from the full solutions to Eq. (10). The condition  $\Lambda(3) = 0$  divides systems whose symmetric mode has the higher frequency (blue) from those whose antisymmetric modes are higher-frequency (red). The latter systems break both parity and time-parity symmetry without periodic driving, as described in Appendix B, and therefore have the defining characteristics of continuous time crystals.

Figures 2(b) and 2(c) present the normal-mode frequencies and growth rates, respectively, obtained from Eq. (10) for a typical family of experimental systems with  $a_1 = 1 \text{ mm}$  ( $x_1 = 0.72$ ). These traces show how the active symmetric mode abruptly crosses over to an active antisymmetric mode at  $\Lambda(3) = 0$ . We demonstrate in Appendix C that the marginally-active antisymmetric state at  $\Lambda(5) = 0$  ( $a_2/a_1 = 2.1$ ) has a linearly stable limit cycle and therefore is a true continuous time crystal.

The model defined by Eq. (6) provides a context for interpreting observations of steady-state oscillations in the experimental system, such as the example in Fig. 1(a). To facilitate this comparison, the particles' measured positions in each video frame are projected along the axis of the acoustic levitator. The common and relative modes are identified from these time traces by principal component analysis, and their frequency content is assessed with the power spectral density,  $S(f)$ , as described in Appendix D. Examples computed from 100 s recordings are plotted in Fig. 3 for two different pairs of spheres.

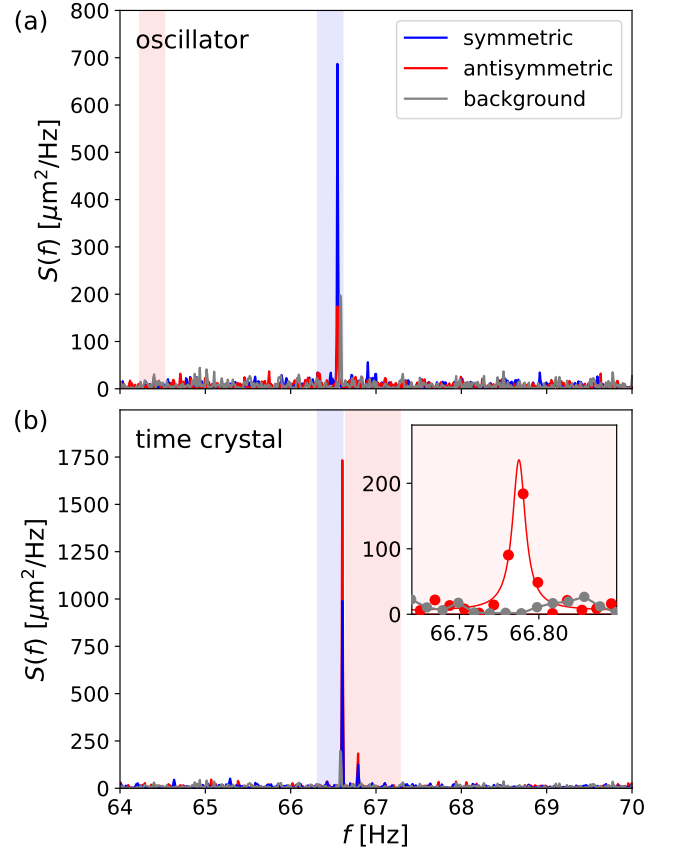


FIG. 3. Power spectral density [39] of the symmetric (blue) and antisymmetric (red) modes of two acoustically-coupled EPS beads in an acoustic levitator. Solid curves are computed from 20 000-frame video sequences acquired at 200 frames/s. Shaded bands indicate the predicted frequency ranges for the normal modes from Eq. (11). Results for a single-particle trajectory (gray) represent the measurement's noise floor. (a) Small particles ( $ka_1 = 0.80 \pm 0.02$  and  $ka_2 = 1.02 \pm 0.02$ ) oscillate in the symmetric mode at the predicted common-mode frequency,  $\Omega_0$ . (b) Larger particles ( $ka_1 = 1.07 \pm 0.04$  and  $ka_2 = 1.21 \pm 0.03$ ) break spatiotemporal symmetry with antisymmetric oscillations at a higher frequency. Inset: Expanded view of the antisymmetric mode's spectral peak (red points) compared with a Lorentzian response (solid red curve) and the measured noise floor (gray points).

The software that implements this analytical pipeline is available in the project's data repository [39]. Analogous results from other pairs of spheres and spot checks of the spheres in Fig. 3 are included in Appendix E.

The data in Fig. 3(a) are obtained with comparatively small spheres, as indicated by the data point in Fig. 2(a), and are predicted to be in the symmetric oscillator state. The larger spheres that produced the data in Fig. 3(b) are predicted to form a time crystal. Shaded regions in Fig. 3 correspond to the ranges of frequencies for the symmetric and antisymmetric modes predicted by Eq. (11) after accounting for experimental uncertainties. The symmetric-mode frequency,  $\text{Im} \left\{ \lambda_{\pm}^{(s)} \right\} = \Omega_0$ , is predicted to be inde-

pendent of the particles' radii and therefore should be the same for both systems in Fig. 3. This is consistent with their observed behavior. The antisymmetric mode of the oscillator in Fig. 1(a) is predicted to have a lower frequency,  $\text{Im}\{\lambda_{\pm}^{(a)}\} < \Omega_0$ , as drawn. No spectral feature is observed at the predicted frequency, however, presumably because the antisymmetric mode is heavily damped. The time crystal in Fig. 3(b) differs from the oscillator by having a higher antisymmetric-mode frequency,  $\text{Im}\{\lambda_{\pm}^{(a)}\} > \Omega_0$ . Indeed, a small peak is observed in the predicted frequency range in Fig. 3(b). The inset to Fig. 3(b) provides a magnified view of this peak and compares it with a Lorentzian,

$$S(f) = \frac{2\tau}{\pi} \frac{S_a}{1 + [2(f - f_a)\tau]^2} + S_{\text{noise}}, \quad (12)$$

where  $f_a = (66.787 \pm 0.004)$  Hz is the antisymmetric mode's center frequency,  $\tau = (100 \pm 10)$  s =  $(6700 \pm 700)$  cycles is the antisymmetric mode's coherence time, and  $S_a/S_{\text{noise}} = 40$  serves as an estimate for the measurement's signal-to-noise ratio. The estimated value of  $\tau$  is comparable to the 108 s duration of the data set and exceeds the system's measured [25] viscous relaxation time,  $(0.16 \pm 0.01)$  s, by orders of magnitude. Sustained oscillations persist for hours longer than the measurement window, which means that the true coherence time of the nonequilibrium steady state may be substantially larger. Comparable results are obtained for other pairs of beads, as reported in Appendix E. Observed normal-mode frequencies fall into narrow bands, which means that the results in Fig. 3 are typical. This is consistent with the prediction that activity precisely compensates dissipation only over a limited range of experimental conditions.

Consistency between the predicted and measured behavior of the levitated two-bead system supports the contention that the experimental system exhibits both active oscillator and active time crystal states, and that both display long-ranged temporal order. This contrasts with previous reports of dissipative time crystals [40] that require either periodic driving [41] or thermal activation [22] to replace energy drained by dissipation. The acoustically levitated system therefore embodies a true classical time crystal [22, 41, 42] that is powered by nonreciprocity and is stabilized by damping [40, 41, 43].

The equations of motion for this system, Eq. (6), also have a fixed-point solution,  $\nu_j = \dot{\nu}_j = 0$ . In this configuration, the forces acting on the spheres are balanced and the spheres are motionless. This is a passive state because the system takes no energy from the standing wave when the spheres are stationary. The oscillatory steady states therefore are a manifestation of emergent activity because the system can exist in active and passive states depending on its configuration. This contrasts with conventional active matter that consumes energy continuously regardless of its configuration.

Emergent activity also arises in larger arrays of acoustically trapped particles. In this context, quenched dis-

order not only creates the conditions required for sustained oscillations, but also can mediate transitions between propagation and localization of linear excitations [44]. Analogous active steady-states should arise in any system where arrays of passive scatterers interact with waves. For example, scattering-mediated emergent activity is likely to explain the classical time crystals recently observed in photonic metamaterials [10, 21] and the collective motions of buoyant particles interacting with capillary waves [45]. Emergent activity therefore provides an unconventional basis for designing compact oscillators, resonant detectors and time bases for technological applications.

## ACKNOWLEDGMENTS

This work was supported by the National Science Foundation under Award Nos. DMR-2104837 and DMR-2428983. The authors acknowledge an exceptionally fruitful exchange of ideas with the three anonymous reviewers in addition to helpful conversations with Vincenzo Vitelli, Paul Chaikin, Ella King, Mathias Casiulis, Andriy Goychuk, Ankit Vyas and Matthew Gronert.

## APPENDICES

### Appendix A: Material Properties

Table I reports material properties for the experiments on acoustically levitated pairs of spheres described in the main text. The same parameters are used in simulations. Properties of air are obtained from Ref. [38]. Reference [25] describes the methods used to measure the force scale,  $F_0$ , of the acoustic trap and the density,  $\rho_j$ , of the levitated particles. Equation numbers refer to definitions of derived quantities in the main text.

### Appendix B: Spatiotemporal symmetry breaking and exceptional points

The main text demonstrates that the antisymmetric-mode frequency for a pair of acoustically levitated particles equals the symmetric-mode frequency for certain particle-size ratios. Specifically, small particles ( $ka_1 = 0.80 \pm 0.02$  and  $ka_2 = 1.02 \pm 0.02$ ) oscillate in the symmetric mode at the predicted common-mode frequency,  $\Omega_0$ , while larger particles ( $ka_1 = 1.07 \pm 0.04$  and  $ka_2 = 1.21 \pm 0.03$ ) break spatiotemporal symmetry with antisymmetric oscillations at a higher frequency. Here we show that the specific spatiotemporal symmetry broken is parity-time ( $PT$ ) symmetry.

TABLE I. Material properties of the experimental system.

Parameter	Symbol	Value	Source
<b>(a) Properties of sound wave</b>			
speed of sound in air	$c_0$	$(343 \pm 1) \text{ m/s}$	measured from node separation
viscosity of air	$\eta_0$	$1.825 \times 10^{-5} \text{ Pa s}$	Ref. [38]
acoustic frequency	$\omega/(2\pi)$	40 kHz	instrumental setting
wave number	$k$	$(732 \pm 1) \text{ rad/m}$	computed
air density	$\rho_0$	$(1.204 \pm 0.005) \text{ kg/m}^3$	Ref. [38]
force scale	$F_0$	$(25.2 \pm 0.3) \mu\text{N}$	Eq. (2b)
<b>(b) Properties of particles</b>			
particle density	$\rho_j$	$(30.5 \pm 0.2) \text{ kg/m}^3$	Ref. [25]
pressure polarizability	$f_{0,j}$	1	estimated
velocity polarizability	$f_{1,j}$	$0.471 \pm 0.002$	Eq. (3b)
<b>(c) Derived dynamical properties</b>			
natural frequency	$\Omega_0/(2\pi)$	$(66.6 \pm 0.6) \text{ Hz}$	Eq. (7)
drag parameter	$\epsilon$	$(1.72 \pm 0.01) \times 10^{-3}$	Eq. (9)
antisymmetric mode frequency factor	$g$	$0.1148 \pm 0.0001$	Eq. (11d)

## 1. Parity symmetry

A system with parity symmetry is one whose dynamics are unchanged upon reflection about a center of symmetry. An example of such a reflection is the exchange of particle identity. Specifically, if a system's dynamics about a fixed point are given by the differential equation

$$\dot{\mathbf{y}} = J\mathbf{y} \quad (\text{B1})$$

with fixed-point Jacobian  $J$ , then approximate parity symmetry corresponds to the condition [46]

$$\|P^{-1}JP - J\| \approx 0, \quad (\text{B2})$$

where  $P$  is the operator that swaps particle identities. Double bars denote the Frobenius norm of the enclosed matrix.

Systems with nonreciprocal interactions, such as a pair of acoustically levitated particles, break parity symmetry by definition. While parity symmetry is always broken when the levitated particles are not identical, parity symmetry can be approximately conserved if  $P$  and  $J$  almost commute. Two acoustically levitated particles, for example, approximately conserve parity symmetry if their size ratio is small ( $a_2/a_1 \leq 2$ ) as shown in Fig. 4(a) and (b). In Fig. 4(a), we observe that the interaction force between two similarly sized particles is repulsive and approximately balanced: the force on particle 1 due to particle 2 is similar in magnitude to the force on particle 2 due to particle 1. This approximate parity symmetry is explicitly observed in Fig. 4(b), which shows the norm difference between the Jacobian and its parity-transform.

Alternatively, parity symmetry can be strongly broken if  $P$  and  $J$  do not commute. In Fig. 4(a), for example, we observe that the interaction force between two very heterogeneous particles ( $a_2/a_1 > 2$ ) is attractive and unbalanced in magnitude. We see this parity violation explicitly in Fig. 4(b), where these dissimilar particles strongly break parity symmetry.

## 2. Parity-time symmetry and exceptional points

While the conservation or violation of parity symmetry describes how energy is transferred between particles, that of parity-time ( $PT$ ) symmetry helps us understand how energy is allocated to our system's dynamical modes. A  $PT$  symmetric system is one whose dynamics are invariant under reflection across an axis of symmetry plus a time reversal. A system with approximate  $PT$  symmetry obeys the condition [46, 47]

$$\|P^{-1}J_D^*P - J_D\| \approx 0, \quad (\text{B3})$$

where the parity operator  $P$  performs a reflection about a center of symmetry and  $J_D^*$  is the complex conjugate of the diagonalized Jacobian,  $J_D$ . When  $PT$  symmetry is broken it can be restored through a limit cycle [48]. If the frequency of this limit cycle is uncorrelated with timescales which appear in the system's equations of motion, the limit cycle realizes a time crystal. Furthermore, in photonics and optics this spontaneously broken  $PT$  symmetry can coincide with the coalescence of two eigenvectors, after which the Jacobian can no longer be diagonalized [47]. These special points, known as “exceptional points”, are typically found in non-Hermitian quantum mechanics [47] and also can arise in nonreciprocal classical systems [48].

Our levitated two-particle system has two dynamical modes describing symmetric and antisymmetric motion. These dynamical modes consist of the two complex conjugate pairs of eigenvalues in main text's Eq. (6) and their corresponding eigenvectors. The relevant parity operator for our system swaps the identity of the eigenvalues within each complex conjugate pair. As long as a unique antisymmetric and symmetric mode exist,  $PT$  symmetry is conserved. Accordingly, in Fig. 4(c) we observe that before and after the bifurcation shown in Fig. 2(b) in the main text, the system of two acoustically levitated particles is approximately  $PT$  symmetric. At the

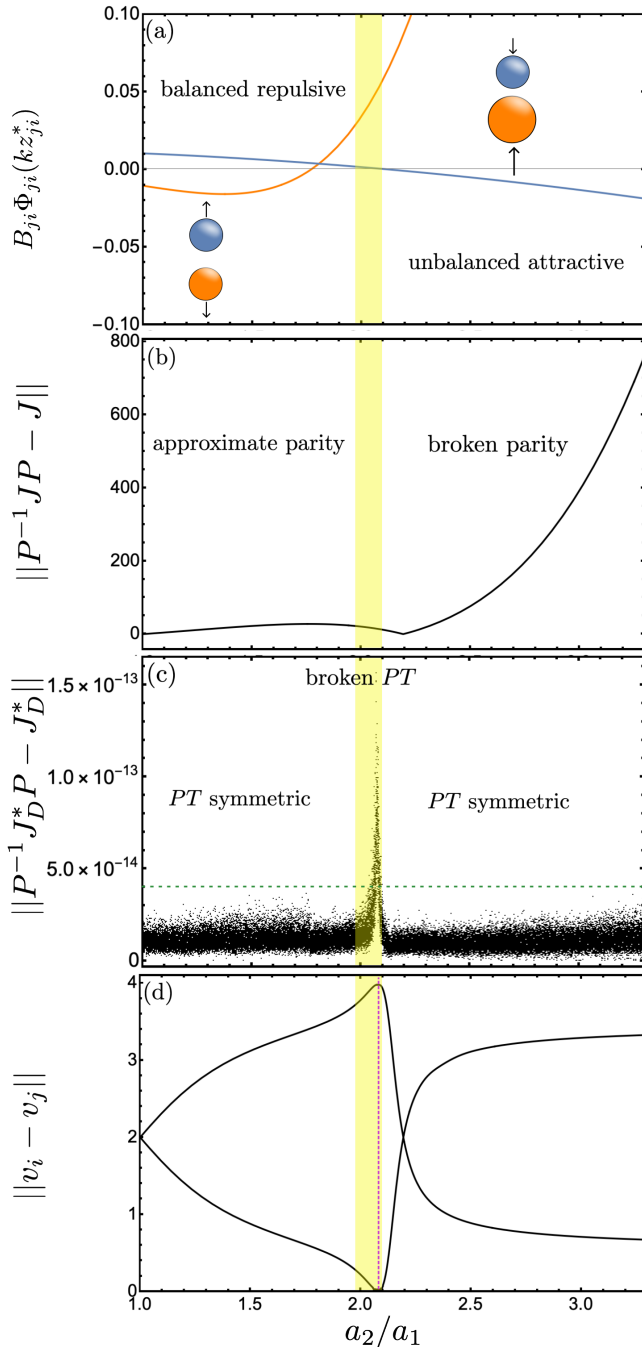


FIG. 4. (a) The fixed point interaction force between two particles of radii  $a_1$  (blue curve) and  $a_2$  (orange curve) as a function of the particle size ratio,  $a_2/a_1$ . When the particle size ratio is small, the interaction force between the particles is repulsive and approximately reciprocal. A large particle size ratio results in an attractive interparticle force that is *nonreciprocal*: the force on particle 2 due to particle 1 is much stronger than the force on particle 1 due to particle 2. The yellow region corresponds to the active region in Fig. 2 in the main text, within which nonreciprocal interactions replace the energy lost to dissipation. (b) The Frobenius norm of the difference between the Jacobian for the levitated two-particle system and the parity-transformed Jacobian as a function of the particle size ratio. Parity is approximately conserved when the interaction force is repulsive. When the interaction force is attractive, parity is strongly broken. (c) The Frobenius norm of the difference between the Jacobian for the levitated two-particle system and the  $PT$ -transformed Jacobian as a function of the particle size ratio.  $PT$ -time symmetry is broken within the (yellow) active range. The horizontal dotted line represents a noise floor below which all norm differences are indistinguishable from zero. (d) The norm difference between all unique pairs of the Jacobian's eigenvectors,  $v_i$ . An exceptional point occurs when the norm difference is zero, as marked by the vertical dotted line. The exceptional point occurs within the active range.

bifurcation in Fig. 2(b) in the main text, however, the symmetric and antisymmetric eigenvalues coalesce and the system strongly breaks  $PT$  symmetry. This spontaneous spatiotemporal symmetry breaking, embodied by the peak in Fig. 4(b), corresponds with the coalescence of two eigenvectors, as shown in Fig. 4(d). The  $PT$  symmetry breaking shown in Fig. 2 therefore coincides with an exceptional point. At this exceptional point, the broken  $PT$  symmetry is restored by a limit cycle, which is the time crystal shown in Fig. 2 of the main text. On this basis, we conclude that the steady-state antisymmetric mode of the dynamical system described by Eq. (6) in

the main text is a continuous classical time crystal.

#### Appendix C: Numerical simulations: Stability of the active dynamical states

Referring to Eq. (6) of the main text, we simulate the dynamics of a pair of acoustically levitated particles by numerically integrating the coupled Langevin equations,

$$\nu_j \equiv \dot{\zeta}_j \quad (C1a)$$

$$\dot{\nu}_j = -\frac{1}{2} \sin(2\zeta_j) - \Gamma_j \nu_j + \sum_{i \neq j} B_{ji} \Phi(\pi + \zeta_2 - \zeta_1) + \xi_j(t), \quad (C1b)$$

with indices  $j = 1, 2$ . The  $j$ -th particle is located at  $\zeta_j$  relative to the node of its acoustic trap in units of the acoustic wavelength. The associated dimensionless velocity is  $\nu_j$ . Dots denote derivatives with respect to time in units of the period of the acoustic traps' natural frequency. Each particle tends to be localized at a node of the standing wave,  $\zeta_j = 0$ , by the primary Gor'kov force. The spheres' motions are damped by viscous drag with dimensionless drag coefficients,  $\Gamma_j = 2\epsilon(ka_j)^2$ , that depends on the spheres' radii,  $a_j$ , relative to the wavelength of sound. The magnitude of the drag force is set by the dimensionless parameter  $\epsilon < 1$ , which is expressed in terms of the system's physical properties in the main text.

Wave-mediated interactions displace the particles from the centers of their traps. These scattering forces depend on the dimensionless interparticle separation through

$$\Phi(kz) = \frac{\cos(kz) + kz \sin(kz)}{(kz)^2}. \quad (C2)$$

The coupling constants,

$$B_{12} = -3 \frac{f_{1,1}^2}{f_{0,1} + f_{1,1}} (ka_2)^3 (1 - \chi_{12}) \quad (C3)$$

$$B_{21} = 3 \frac{f_{1,2}^2}{f_{0,2} + f_{1,2}} (ka_1)^3 (1 - \chi_{21}), \quad (C4)$$

incorporate the coefficients,

$$\chi_{ij} = \frac{1}{2} (ka_i)^2 \left( 1 + \frac{3}{5} \frac{a_j^2}{a_i^2} \right) \quad (C5)$$

to order  $(ka_j)^5$  in the multipole expansion for the interparticle interaction. This result for the axial König interaction between dissimilar pairs of spheres is one of the original contributions of this work. The pair interaction is nonreciprocal when  $B_{12} \neq -B_{21}$ , which is the case when the particles are composed of the same material but have different radii. The simulated particles also are subject to Gaussian random forces with correlations

$$\langle \xi_i(t) \xi_j(0) \rangle = 2s^2 \delta_{ij} \delta(t), \quad (C6)$$

that are characterized by a dimensionless amplitude of order  $s \approx 10^{-3}$ . This small amount of noise is intended to assess the linear stability of the dynamical states identified in the main text. It is not intended to model thermal noise or environmental perturbations.

A simulation is configured with six dimensionless parameters:  $ka_1$  and  $ka_2$ ,  $B_{12}$ , and  $B_{21}$ , the drag coefficient  $\epsilon$ , and the noise coefficient  $s$ . These parameters can be

related to the physical properties of an experimental system through the values tabulated in Table I. For comparison with the experiments described in the main text, we choose  $a_1 = 1 \text{ mm}$  ( $ka_1 = 0.732$ ) and  $a_2 > a_1$ . We integrate this system of equations with the fourth-order Runge-Kutta method implemented in the `solve_ivp` routine that is provided by `scipy.integrate` [49]. Typical trajectories and their Poincaré sections appear in Fig. 5.

In the absence of noise, the null vector,  $\nu_j = \dot{\nu}_j = 0$ , is a solution of Eq. (C1) for any pair of spheres that can be stably trapped. This fixed point corresponds to a set of particle positions,  $\zeta_j$  and  $\zeta_i$ , that satisfy

$$\frac{1}{2} \sin(2\zeta_j) = \sum_{i \neq j} B_{ji} \Phi(kz_{ji}). \quad (C7)$$

The system neither dissipates energy in this configuration nor extracts energy from the standing wave. Such a fixed point therefore is a passive state.

Figure 5 presents numerically evaluated results for a pair of acoustically levitated spheres under conditions specified in Table II. The first column in Fig. 5 shows the trajectory of particle 1,  $\zeta_1(t)$ , starting from an arbitrary displacement,  $\zeta_1(0) = -0.01$  and  $\zeta_2(0) = 0.01$ . The second column shows Poincaré sections of the two-particle trajectories in the  $\zeta_2$ - $\zeta_2$  plane obtained when particle 1 passes through its equilibrium position with  $\zeta_1 = 0$ .

Figure 5(a) shows a typical oscillator state in which the pair trajectory rings down to a static equilibrium. The particles' nonreciprocal interactions do not provide enough energy to compensate for dissipation under these conditions and the system tends toward its fixed point. The fixed point is stable for such a system.

The active time-crystal state in Fig. 5(b) shows how a two-particle system behaves when nonreciprocity precisely compensates for drag. In this case, the system selects a steady-state amplitude and the Poincaré map converges on a state in which particle 2 remains in motion. Precise matching of activity and drag is achieved for particle sizes satisfying  $\Lambda(5) = 0$ , as explained in the main text. The prediction that such a system constitutes a true time crystal is consistent with the results of this simulation. The system also converges on the same steady-state time-crystal solution for other choices of the initial positions in the range  $\zeta_1, \zeta_2 \in (-0.5, 0.5)$ .

The continuous time-crystal persists even in the presence of random force noise, as shown in Fig. 5(c). This result incorporates a comparatively large amount of noise,  $s = 10^{-3}$ . The Poincaré map nevertheless converges into a region around the same limit cycle observed in Fig. 5(b). This demonstrates that the true time-crystal state is linearly stable against perturbations. Larger amplitudes of noise,  $s \gtrsim 10^{-2}$ , destabilize the time crystal state and can disrupt the two-particle system altogether by enabling one or both of the particles to escape their traps.

TABLE II. Parameters used in Fig. 5. Particle 1 radius:  $a_1 = 1$  mm; particle 1 drag coefficient:  $\Gamma_1 = 6.5 \times 10^{-3}$ .

	$a_2$	$\Gamma_2$	$B_{12}$	$B_{21}$	$s$
Figure 5(a)	1.5 mm	$2.9 \times 10^{-3}$	$-2.2 \times 10^{-1}$	$4.2 \times 10^{-2}$	0
Figure 5(b)	2.12 mm	$1.5 \times 10^{-3}$	$-1.3 \times 10^{-2}$	$-6.6 \times 10^{-2}$	0
Figure 5(c)	2.12 mm	$1.5 \times 10^{-3}$	$-1.3 \times 10^{-2}$	$-6.6 \times 10^{-2}$	$10^{-3}$

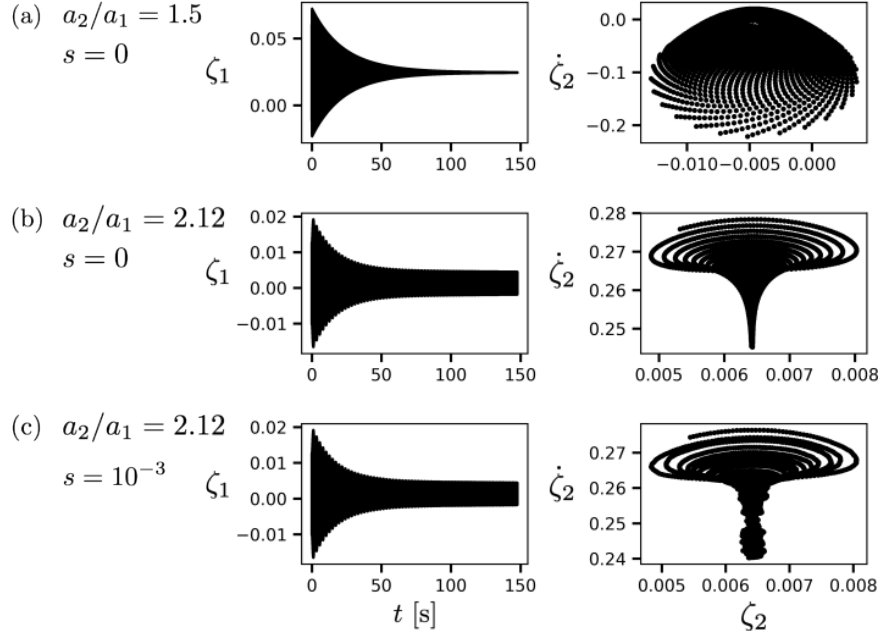


FIG. 5. Numerical solutions and Poincaré maps of Eq. (C1) for two-particle systems with  $a_1 = 1$  mm. (a)  $a_2 = 1.5$  mm: In the absence of noise ( $s = 0$ ), the system's oscillations ring down to a stable fixed point ( $\dot{\zeta}_1 = \dot{\zeta}_2 = 0$ ). (b)  $a_2 = 2.12$  mm,  $s = 0$ : Analytically predicted conditions for a true time crystal. The trajectory starts from rest and evolves toward a steady-state limit cycle corresponding to the true continuous time crystal. (c)  $a_2 = 2.12$  mm,  $s = 10^{-3}$ : A small amount of additive force noise does not prevent the system from evolving toward the steady-state limit cycle, confirming that the time crystal is linearly stable.

#### Appendix D: Experimental time series analysis

Data and analysis code used to create the figures in the main text are available from OSF repository [39]. Figure 6(a) shows the measured trajectories,  $z_1(t)$  and  $z_2(t)$ , for the two spheres in the steady-state time crystal presented in Fig. 3(b) of the main text. Each sphere is located to within 0.3 pixel (40  $\mu\text{m}$ ) in each video frame by thresholding the image and finding the center of mass of each of the the simply-connected islands of pixels. This analysis also yields estimates for the particles' radii. Figure 6(b) shows a 300 ms time window in which the individual particles' fluctuations are more clearly visible.

The pair's normal modes are estimated from the full 20 000-step time series using the python implementation of principal component analysis provided by the `sklearn.decomposition` library of `scikit-learn` [50]. Figure 6(c) shows the result of that decomposition over the same time window presented in Fig. 6(b).

The power spectral density for each normal-mode signal is computed using Welch's method [51] as imple-

mented in `scipy.signal` [49]. A typical time series consisting of 20 000 pair positions acquired at 200 frames/s yields an effective frequency resolution of 0.01 Hz. Figure 7 shows the power spectral densities from Fig. 3 of the main text replotted on a semilogarithmic scale over a wider range of frequencies. Blue traces show contributions to the symmetric modes obtained from principal component analysis of the pair trajectories, and red traces show contributions to the antisymmetric modes. Vertical blue and red bars represent the predicted range of normal-mode frequencies for symmetric and antisymmetric modes, respectively. Gray traces in Fig. 7 show the power spectral densities for the trajectory of a single sphere trapped in one node of the acoustic levitator. This establishes the noise floor for the measurement and is consistent with the observed background for the two-particle normal modes.

In addition to sustained oscillations at the predicted symmetric-mode and antisymmetric-mode frequencies, the system presented in Fig. 7(b) also displays strong broad-band spectral features at lower frequencies in its

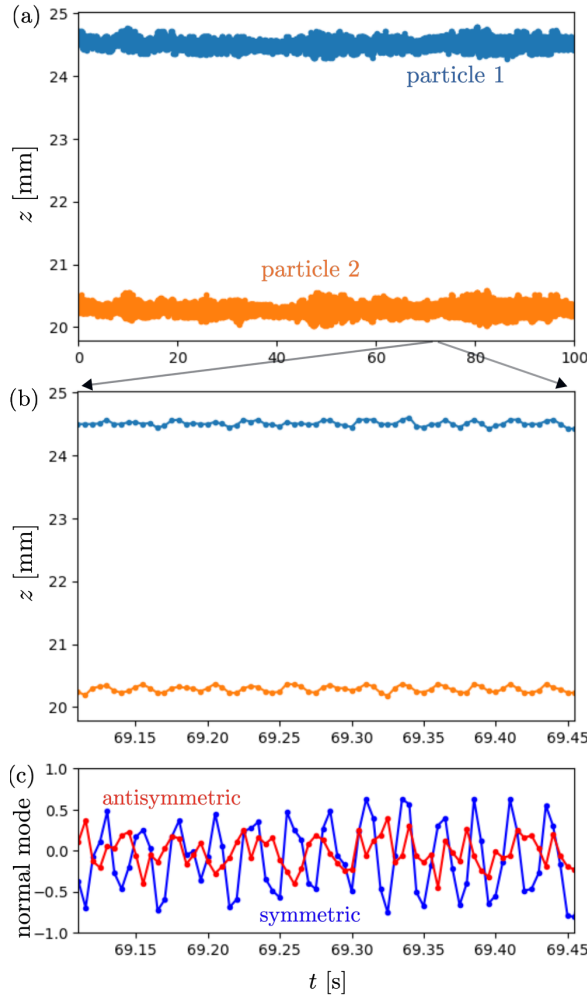


FIG. 6. (a) Measured trajectories of the pair of levitated EPS beads presented in Fig. 3(b) of the main text. (b) Detail of the time series showing the particles' coherent oscillations. (c) Symmetric (blue) and antisymmetric (red) components of the trajectory data from (b).

common-mode motion (blue curve). These low-frequency spectral features result from coupling between the particles' axial and transverse degrees of freedom arising from the overall large amplitude of these particles' oscillations. The particles' transverse displacements are not accounted for by Eq. (6), which is a one-dimensional model. The acoustic levitator's traps are weaker in the transverse direction than in the axial direction, which means that transverse displacements occur at lower frequencies and

with larger amplitudes than coherent axial oscillations. The axial and transverse modes are linearly independent for small-amplitude oscillations. At larger amplitudes, however, the nonlinearity of the trapping potential couples transverse displacements into the axial degrees of freedom, leading to the observed broad response. Interpreting these observations in light of the one-dimensional theory, we propose that the antisymmetric mode is actively powered under the conditions of Fig. 7(b) and that

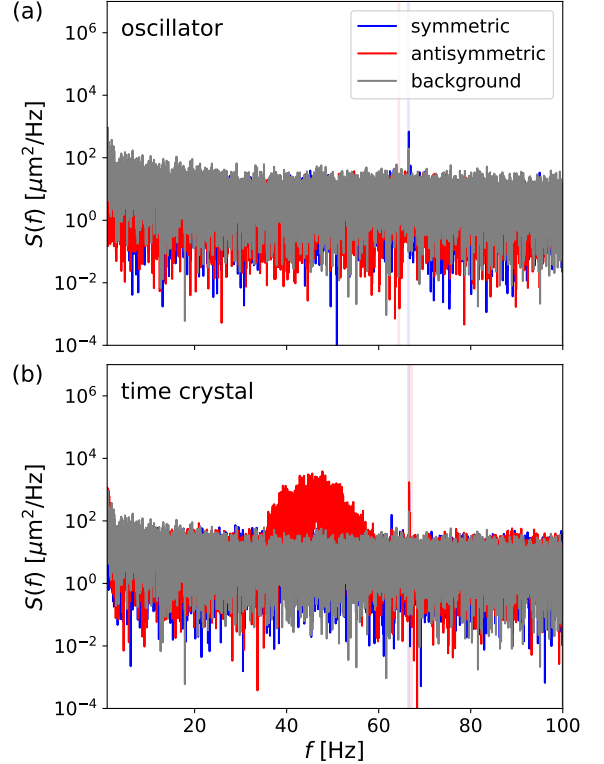


FIG. 7. Power spectra for the pairs of particles reported in Fig. 3 of the main text, replotted on semilogarithmic axes over a larger frequency range. (a) Active oscillator showing strong oscillations at the predicted symmetric-mode frequency, plotted as a (blue) vertical shaded bar. No response is apparent at the frequency for the antisymmetric mode (red). (b) Steady-state time crystal displaying a spectral peak at the predicted frequency for antisymmetric oscillations (red). Large-amplitude in-line oscillations excite transverse oscillations that contribute to the broad low-frequency response in the symmetric mode (blue).

energy from that mode is then nonlinearly coupled into other degrees of freedom.

#### Appendix E: Additional data sets

In addition to the two datasets showcased in the main text, Fig. 8 presents power spectral densities for eight additional datasets, each obtained from 20 000-frame video sequences acquired at 200 frames/s. The four datasets presented in Fig. 8A and Fig. 8B show results comparable to those in Fig. 3 in the main text but for other pairs of particles. Agreement between observed and predicted normal-mode frequencies add support to the claimed predictive power of the one-dimensional dynamical model presented in the main text.

The other four datasets displayed in Figs. 8C and 8D are obtained for the same pairs of particles used in Fig. 3, but from video sequences obtained 5 min later. These power spectral densities yield normal-mode frequencies in agreement with those presented in Fig. 3, supporting the claim that these systems are in nonequilibrium steady-states.

For each dataset, the power spectral density for the symmetric mode is plotted in blue and that for the antisymmetric mode is plotted in red. Results for the smaller of the two particles stably trapped in isolation are plotted in gray and provide an estimate for the measurements' noise floor. Colored bands represent the predicted normal-mode frequencies of the symmetric and antisymmetric modes based on the particles' measured sizes and the material properties tabulated in Table I. Insets provide a zoomed-in view of the antisymmetric mode under conditions that are predicted to support a time crystal. Solid curves are fits to a Lorentzian line shape for the peak height, the noise floor and the persistence time of the antisymmetric mode.

The symmetric-mode frequency for every pair of particles is consistent with the natural frequency,  $\Omega_0$ , as predicted in the main text. The antisymmetric-mode frequency is predicted to be lower than  $\Omega_0$  in the active-oscillator state, although no significant spectral peaks are observed within the predicted range. This observation is consistent with the prediction that the antisymmetric mode is highly damped under conditions that support a steady-state active oscillator.

The antisymmetric-mode frequency in a steady-state time crystal is predicted to exceed  $\Omega_0$ . Spectral peaks in the range of predicted antisymmetric-mode frequencies are observed for all pairs of particles whose sizes support a steady-state time crystal.

All experimental results from the main text and these additional data sets and their metadats are summarized in Tables III-VI. Data and analysis files for all datasets are available for download at Ref. [39].

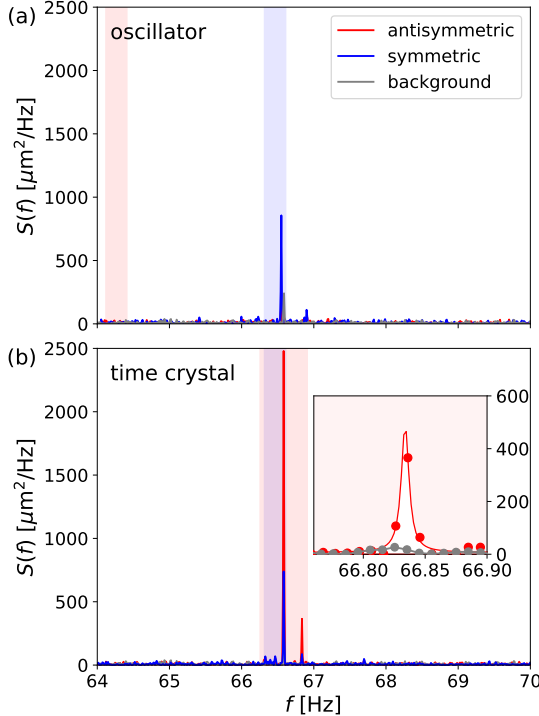


FIG. 8A (a) Active oscillator:  $ka_1 = 0.74 \pm 0.03$  and  $ka_2 = 1.02 \pm 0.02$ . (b) Time crystal:  $ka_1 = 1.03 \pm 0.05$  and  $ka_2 = 1.22 \pm 0.02$ .

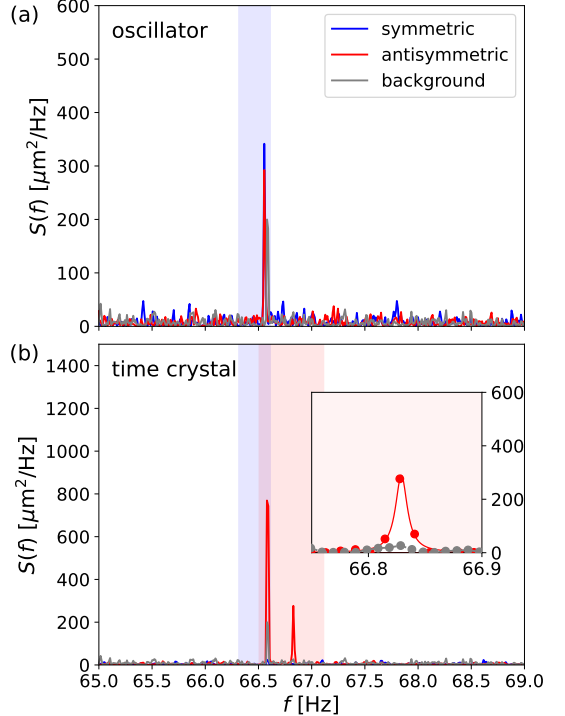


FIG. 8B (a) Active oscillator:  $ka_1 = 0.82 \pm 0.02$  and  $ka_2 = 1.02 \pm 0.02$ . (b) Time crystal:  $ka_1 = 1.10 \pm 0.03$  and  $ka_2 = 1.17 \pm 0.04$ .

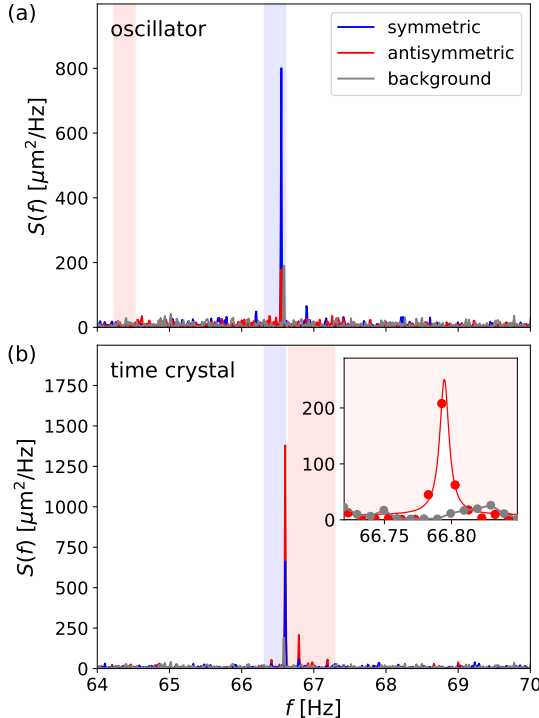


FIG. 8C (a) Active oscillator:  $ka_1 = 0.80 \pm 0.02$  and  $ka_2 = 1.02 \pm 0.02$ . (b) Time crystal:  $ka_1 = 1.07 \pm 0.04$  and  $ka_2 = 1.21 \pm 0.03$ .

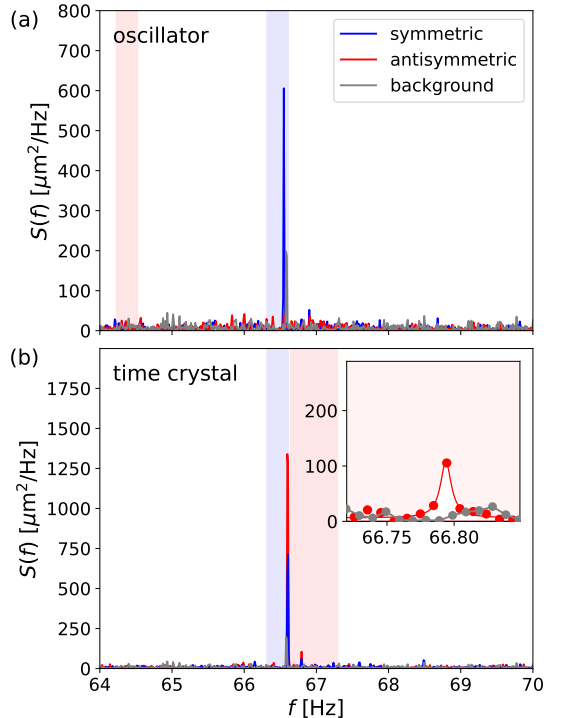


FIG. 8D (a) Active oscillator:  $ka_1 = 0.80 \pm 0.02$  and  $ka_2 = 1.02 \pm 0.02$ . (b) Time crystal:  $ka_1 = 1.07 \pm 0.04$  and  $ka_2 = 1.21 \pm 0.03$ .

FIG. 8. Power spectral densities for additional data sets.

### Appendix F: Tables of experimental results

The videos, trajectory data and analysis code for the experimental realizations described in this work are freely available in a public data repository [39]. Table III numbers the experimental realizations and associates each video with the associated tracking data and analysis code.

Tables IV, V, and VI summarize the experimental conditions and analytical outcomes for each of these experiments.

TABLE III. Summary of experiments and associated tracking and analysis files.

Experiment	Data file	Analysis file
#	Tracking (.csv) and raw (.avi) filestem	Analysis (.ipynb) filestem
1	oscillationsgreensmall02	powerspectrum_final
2	oscillationsblueyellowbig03	powerspectrum_final
3	oscillationsgreengreensmall	powerspectrum_final02
4	oscillationsorangebluebig03	powerspectrum_final02
5	oscillationsgreenpeachsmall03	powerspectrum_final03
6	oscillationsblueredbig	powerspectrum_final03
7	oscillationsgreensmall03	powerspectrum_final_sc02
8	oscillationsblueyellowbig02	powerspectrum_final_sc02
9	oscillationsgreensmall	powerspectrum_final_sc03
10	oscillationsblueyellowbig	powerspectrum_final_sc03

TABLE IV. Experimental parameters in the oscillator and time-crystal regimes.

Parameter	Description	Exp. 1	Exp. 2	Exp. 3	Exp. 4
$ka_1$	reduced particle 1 radius	$0.80 \pm 0.02$	$1.07 \pm 0.04$	$0.74 \pm 0.03$	$1.03 \pm 0.05$
$ka_2$	reduced particle 2 radius	$1.02 \pm 0.02$	$1.21 \pm 0.03$	$1.02 \pm 0.02$	$1.22 \pm 0.02$
$f_s^{(\text{theory})}$	symmetric freq. (theory)	$(66.5 \pm 0.3)$ Hz			
$f_a^{(\text{theory})}$	antisymmetric freq. (theory)	$(64.4 \pm 0.3)$ Hz	$(67.0 \pm 0.6)$ Hz	$(64.3 \pm 0.3)$ Hz	$(66.6 \pm 0.7)$ Hz
$f_s^{(\text{data})}$	symmetric freq. (data)	66.5 Hz	66.6 Hz	66.6 Hz	66.6 Hz
$f_a^{(\text{data})}$	antisymmetric freq. (data)	n/a	66.8 Hz	n/a	66.8 Hz
$t_c$	time crystal coherence time	n/a	$(102 \pm 14)$ s	n/a	$(134 \pm 28)$ s
SNR	time crystal signal/noise ratio	n/a	42	n/a	71
$T$	length of video	104 s	108 s	103 s	103 s
Identity	oscillator (O)/time crystal (TC)	O	TC	O	TC
Figure	used in figure panel(s)	3(a)	3(b)	8A(a)	8A(b)

TABLE V. Experimental parameters in the oscillator and time-crystal regimes.

Parameter	Description	Exp. 5	Exp. 6	Exp. 7	Exp. 8
$ka_1$	reduced particle 1 radius	$0.82 \pm 0.02$	$1.10 \pm 0.03$	$0.80 \pm 0.02$	$1.07 \pm 0.04$
$ka_2$	reduced particle 2 radius	$1.02 \pm 0.02$	$1.17 \pm 0.04$	$1.02 \pm 0.02$	$1.21 \pm 0.03$
$f_s^{(\text{theory})}$	symmetric freq. (theory)	$(66.5 \pm 0.3)$ Hz			
$f_a^{(\text{theory})}$	antisymmetric freq. (theory)	$(64.4 \pm 0.3)$ Hz	$(66.8 \pm 0.6)$ Hz	$(63.4 \pm 0.1)$ Hz	$(67.0 \pm 0.6)$ Hz
$f_s^{(\text{data})}$	symmetric freq. (data)	66.6 Hz	66.6 Hz	66.6 Hz	66.6 Hz
$f_a^{(\text{data})}$	antisymmetric freq. (data)	n/a	66.8 Hz	n/a	66.8 Hz
$t_c$	time crystal coherence time	n/a	$(80 \pm 8)$ s	n/a	$(120 \pm 36)$ s
SNR	time crystal signal/noise ratio	n/a	1541	n/a	30
$T$	length of video	102 s	77 s	110 s	101 s
Identity	oscillator (O)/time crystal (TC)	O	TC	O	TC
Figure	used in figure panel(s)	8B(a)	8B(b)	8C(a)	8C(b)

TABLE VI. Experimental parameters in the oscillator and time-crystal regimes.

Parameter	Description	Exp. 9	Exp. 10
$ka_1$	reduced particle 1 radius	$0.80 \pm 0.02$	$1.07 \pm 0.04$
$ka_2$	reduced particle 2 radius	$1.02 \pm 0.02$	$1.21 \pm 0.03$
$f_s^{(\text{theory})}$	symmetric freq. (theory)	$(66.5 \pm 0.3)$ Hz	$(66.5 \pm 0.3)$ Hz
$f_a^{(\text{theory})}$	antisymmetric freq. (theory)	$(64.4 \pm 0.3)$ Hz	$(67.0 \pm 0.7)$ Hz
$f_s^{(\text{data})}$	symmetric freq. (data)	66.6 Hz	66.6 Hz
$f_a^{(\text{data})}$	antisymmetric freq. (data)	n/a	66.8 Hz
$t_c$	time crystal coherence time	n/a	$(101 \pm 16)$ s
SNR	time crystal signal/noise ratio	n/a	17
$T$	length of video	105 s	102 s
Identity	oscillator (O)/time crystal (TC)	O	TC
Figure	used in figure panel(s)	8D(a)	8D(b)

- 
- [1] M. M. Burns, J.-M. Fournier, and J. A. Golovchenko, Optical binding, *Phys. Rev. Lett.* **63**, 1233 (1989).
- [2] M. M. Burns, J.-M. Fournier, and J. A. Golovchenko, Optical matter: crystallization and binding in intense optical fields, *Science* **249**, 749 (1990).
- [3] P. Marston, E. Trinh, J. Depew, and J. Asaki, Response of bubbles to ultrasonic radiation pressure: Dynamics in low gravity and shape oscillations, in *Bubble Dynamics and Interface Phenomena*, Fluid Mechanics and its Applications, Vol. 23, edited by J. Blake, J. Boulton-Stone, and N. Thomas (Springer Science+Business Media, 1994) pp. 343–353.
- [4] D. Rabaud, P. Thibault, M. Mathieu, and P. Marmottant, Acoustically bound microfluidic bubble crystals, *Phys. Rev. Lett.* **106**, 134501 (2011).
- [5] A. Doinikov and S. Zavtrak, On the “bubble grapes” induced by a sound field, *J. Acoust. Soc. Am.* **99**, 3849 (1996).
- [6] M. X. Lim, B. VanSaders, A. Souslov, and H. M. Jaeger, Mechanical properties of acoustically levitated granular rafts, *Phys. Rev. X* **12**, 021017 (2022).
- [7] M. X. Lim, B. VanSaders, and H. M. Jaeger, Acoustic manipulation of multi-body structures and dynamics, *Rep. Prog. Phys.* **87**, 064601 (2024).
- [8] S. Sukhov, A. Shalin, D. Haefner, and A. Dogariu, *Actio et reactio in optical binding*, *Opt. Express* **23**, 247 (2015).
- [9] S. Sukhov and A. Dogariu, Non-conservative optical forces, *Rep. Prog. Phys.* **80**, 112001 (2017).
- [10] V. Raskatla, T. Liu, J. Li, K. F. MacDonald, and N. I. Zheludev, Continuous space-time crystal state driven by nonreciprocal optical forces, *Phys. Rev. Lett.* **133**, 136202 (2024).
- [11] E. M. King, M. C. Morrell, J. B. Sustiel, M. Gronert, H. Pastor, and D. G. Grier, Scattered waves fuel emergent activity, *Phys. Rev. Research* **7**, 013055 (2025).
- [12] S. Ramaswamy, The mechanics and statistics of active matter, *Annu. Rev. Condens. Matter Phys.* **1**, 323 (2010).
- [13] M. C. Marchetti, J.-F. Joanny, S. Ramaswamy, T. B. Liverpool, J. Prost, M. Rao, and R. A. Simha, Hydrodynamics of soft active matter, *Rev. Mod. Phys.* **85**, 1143 (2013).
- [14] C. Bechinger, R. Di Leonardo, H. Löwen, C. Reichhardt, G. Volpe, and G. Volpe, Active particles in complex and crowded environments, *Rev. Mod. Phys.* **88**, 045006 (2016).
- [15] S. Shankar, A. Souslov, M. J. Bowick, M. C. Marchetti, and V. Vitelli, Topological active matter, *Nat. Rev. Phys.* **4**, 380 (2022).
- [16] M. te Vrugt, B. Liebchen, and M. E. Cates, What exactly is ‘active matter’? (2025), arXiv:2507.21621 [cond-mat.soft].
- [17] H. Sompolinsky and I. Kanter, Temporal association in asymmetric neural networks, *Phys. Rev. Lett.* **57**, 2861 (1986).
- [18] R. Mandal, R. Huang, M. Fruchart, P. G. Moerman, S. Vaikuntanathan, A. Murugan, and V. Vitelli, Learning dynamical behaviors in physical systems (2024), arXiv:2406.07856 [cond-mat.soft].
- [19] C. Weis, M. Fruchart, R. Hanai, K. Kawagoe, P. B. Littlewood, and V. Vitelli, Coalescence of attractors: Exceptional points in non-linear dynamical systems (2022), arXiv:2207.11667 [nlin.CD].
- [20] M. P. Zaletel, M. Lukin, C. Monroe, C. Nayak, F. Wilczek, and N. Y. Yao, Colloquium: Quantum and classical discrete time crystals, *Rev. Mod. Phys.* **95**, 031001 (2023).
- [21] T. Liu, J.-Y. Ou, K. F. MacDonald, and N. I. Zheludev, Photonic metamaterial analogue of a continuous time crystal, *Nat. Phys.* **19**, 986 (2023).
- [22] N. Y. Yao, C. Nayak, L. Balents, and M. P. Zaletel, Classical discrete time crystals, *Nat. Phys.* **16**, 438 (2020).
- [23] A. Marzo, A. Barnes, and B. W. Drinkwater, TinyLev: A multi-emitter single-axis acoustic levitator, *Rev. Sci. Instr.* **88**, 085105 (2017).
- [24] M. A. Abdelaziz and D. G. Grier, Acoustokinetics: Crafting force landscapes from sound waves, *Phys. Rev. Research* **2**, 013172 (2020).
- [25] M. Morrell and D. G. Grier, Acoustodynamic mass determination: Accounting for inertial effects in acoustic levitation of granular materials, *Phys. Rev. E* **108**, 064903 (2023).
- [26] K. Yoshioka and Y. Kawasima, Acoustic radiation pressure on a compressible sphere, *Acta Acust. United Ac.* **5**, 167 (1955).
- [27] L. Gor’kov, On the forces acting on a small particle in an acoustical field in an ideal fluid, *Sov. Phys. Dokl.* **6**, 773 (1962).
- [28] A. A. Doinikov, Acoustic radiation pressure on a rigid sphere in a viscous fluid, *Proc. R. Soc. Lond. A* **447**, 447–466 (1994).
- [29] J. Horvath, Expanded polystyrene (EPS) geofoam: an introduction to material behavior, *Geotext. Geomembr.* **13**, 263 (1994).
- [30] W. König, Hydrodynamisch-akustische Untersuchungen, *Ann. Phys.* **279**, 43 (1891).
- [31] M. Settnes and H. Bruus, Forces acting on a small particle in an acoustical field in a viscous fluid, *Phys. Rev. E* **85**, 016327 (2012).
- [32] N. St. Clair, D. Davenport, A. D. Kim, and D. Kleckner, Dynamics of acoustically bound particles, *Phys. Rev. Res.* **5**, 013051 (2023).
- [33] X. Zheng and R. E. Apfel, Acoustic interaction forces between two fluid spheres in an acoustic field, *J. Acoust. Soc. Am.* **97**, 2218 (1995).
- [34] G. T. Silva and H. Bruus, Acoustic interaction forces between small particles in an ideal fluid, *Phys. Rev. E* **90**, 063007 (2014).
- [35] M. R. Maxey and J. J. Riley, Equation of motion for a small rigid sphere in a nonuniform flow, *Phys. Fluids* **26**, 883 (1983).
- [36] L. Landau and E. Lifshitz, *Fluid Mechanics*, Course of Theoretical Physics, Vol. 6 (Pergamon, 2013).
- [37] E. Hinch, *Perturbation Methods*, Cambridge Texts in Applied Mathematics (Cambridge University Press, 1991).
- [38] D. Lide, ed., *CRC Handbook of Chemistry and Physics*, 104th ed. (Taylor & Francis, 2017).
- [39] M. Morrell and D. G. Grier, OSF: Nonreciprocal wave-mediated interactions power classical a time crystal (2025), <https://dx.doi.org/10.17605/OSF.IO/SX7UG>.
- [40] H. Keßler, P. Kongkhambut, C. Georges, L. Mathey, J. G. Cosme, and A. Hemmerich, Observation of a dissipative time crystal, *Phys. Rev. Lett.* **127**, 043602 (2021).

- [41] H. Taheri, A. B. Matsko, L. Maleki, and K. Sacha, All-optical dissipative discrete time crystals, *Nat. Commun.* **13**, 848 (2022).
- [42] A. Shapere and F. Wilczek, Classical time crystals, *Phys. Rev. Lett.* **109**, 160402 (2012).
- [43] K. Sacha and J. Zakrzewski, Time crystals: a review, *Rep. Prog. Phys.* **81**, 016401 (2017).
- [44] P. Sheng, *Scattering and Localization of Classical Waves in Random Media*, Series in Computer Science (World Scientific, 1990).
- [45] I. Ho, G. Pucci, A. U. Oza, and D. M. Harris, Capillary surfers: Wave-driven particles at a vibrating fluid interface, *Phys. Rev. Fluids* **8**, L112001 (2023).
- [46] R. Shankar, *Principles of Quantum Mechanics* (Springer, 1994).
- [47] M. A. Miri and A. Alù, Exceptional points in optics and photonics, *Science* **363** (2019).
- [48] M. Fruchart, R. Hanai, P. B. Littlewood, and V. Vitelli, Non-reciprocal phase transitions, *Nature* **592**, 363 (2021).
- [49] P. Virtanen, R. Gommers, T. E. Oliphant, M. Haberland, T. Reddy, D. Cournapeau, E. Burovski, P. Peterson, W. Weckesser, J. Bright, S. J. van der Walt, M. Brett, J. Wilson, K. J. Millman, N. Mayorov, A. R. J. Nelson, E. Jones, R. Kern, E. Larson, C. J. Carey, İ. Polat, Y. Feng, E. W. Moore, J. VanderPlas, D. Laxalde, J. Perktold, R. Cimrman, I. Henriksen, E. A. Quintero, C. R. Harris, A. M. Archibald, A. H. Ribeiro, F. Pedregosa, P. van Mulbregt, and SciPy 1.0 Contributors, SciPy 1.0: Fundamental Algorithms for Scientific Computing in Python, *Nat. Methods* **17**, 261 (2020).
- [50] F. Pedregosa, G. Varoquaux, A. Gramfort, V. Michel, B. Thirion, O. Grisel, M. Blondel, P. Prettenhofer, R. Weiss, V. Dubourg, J. Vanderplas, A. Passos, D. Cournapeau, M. Brucher, M. Perrot, and E. Duchesnay, Scikit-learn: Machine learning in Python, *J. Mach. Learn. Res.* **12**, 2825 (2011).
- [51] P. Welch, The use of fast Fourier transform for the estimation of power spectra: A method based on time averaging over short, modified periodograms, *IEEE Trans. Audio Electroacoust.* **15**, 70 (2003).